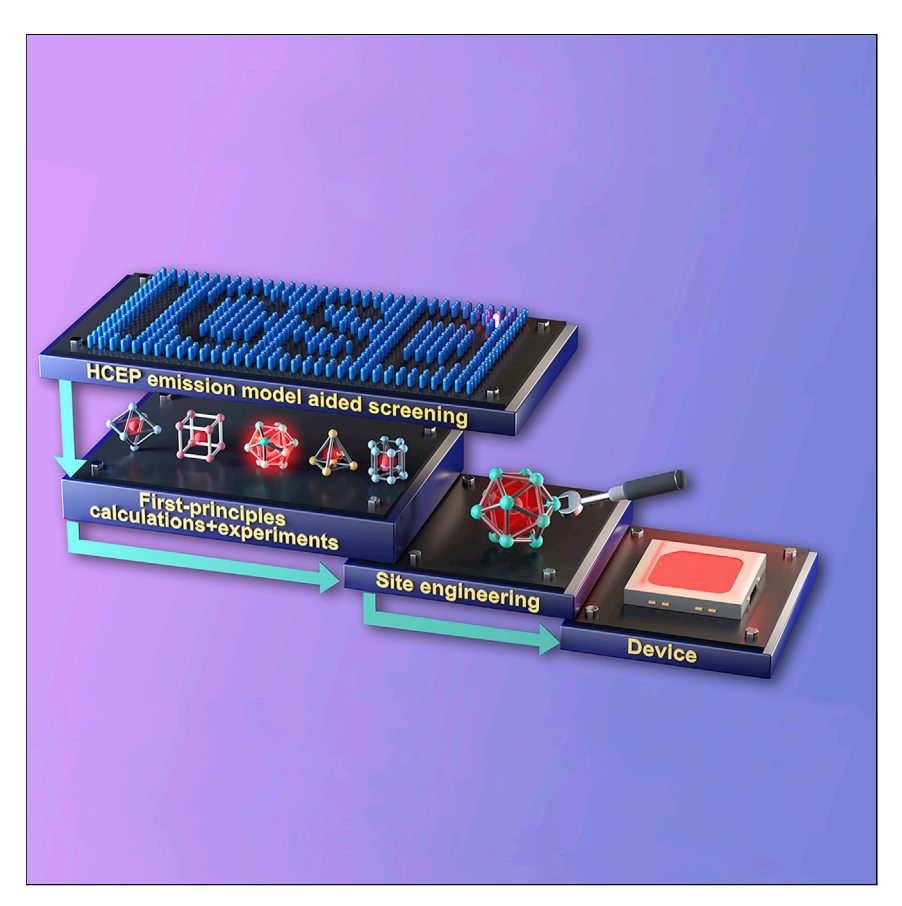
Matter



Article

Efficient near-infrared phosphors discovered by parametrizing the Eu(II) 5*d*-to-4*f* energy gap



Using this harmonic covalo-electrostatic parameterization (HCEP) model, a cost-efficient high-throughput screening of nitride materials from the Inorganic Crystal Structure Database (ICSD) identifies five potential Eu(II)-activated NIR phosphors, which were then experimentally validated. Subsequently, we performed targeted spectral optimizations based on a photoluminescence design map of Eu(II)-activated phosphors. By using the developed Eu(II)-activated phosphors, we further fabricated a prototype NIR device that shows excellent optical powers, surpassing the current counterparts.

Shuxing Li, Mahdi Amachraa, Chi Chen, Le Wang, Zhenbin Wang, Shyue Ping Ong, Rong-Jun Xie

z9wang@eng.ucsd.edu (Z.W.) ongsp@eng.ucsd.edu (S.P.O.) rjxie@xmu.edu.cn (R.-J.X.)

Highlights

An emission wavelength prediction model for Eu(II)-activated phosphors

Eu(II)-activated phosphors with ultralong emission and high quantum efficiency

In silico property-targeted design capability for novel Eu(II)-activated phosphors



Benchmark

First qualification/assessment of material properties and/or performance

Li et al., Matter 5, 1–13 June 1, 2022 © 2022 Elsevier Inc. https://doi.org/10.1016/j.matt.2022.04.009

Matter



Article

Efficient near-infrared phosphors discovered by parametrizing the Eu(II) 5*d*-to-4*f* energy gap

Shuxing Li,^{1,4} Mahdi Amachraa,^{2,4} Chi Chen,² Le Wang,³ Zhenbin Wang,^{2,*} Shyue Ping Ong,^{2,*} and Rong-Jun Xie^{1,5,*}

SUMMARY

Inorganic materials with rare-earth activators (e.g., Ce, Eu) exhibit broad 5d-to-4f emission spectra characterized by a strong host material dependency. Despite extensive research, the development of an efficient and near-infrared (NIR) 5d-to-4f emission remains elusive. Herein, we introduce key descriptors of the Eu(II)-host interactions and predict the in-crystal 5d-to-4f energy gap with a rootmean-square error of ca. 0.03 eV (7.0 nm). By incorporating this luminescence predictor into a high-throughput screening of 223 nitride materials in the Inorganic Crystal Structure Database, we identify and experimentally validate (Sr,Ba)₃Li₄Si₂N₆:Eu(II) with NIR emissions of λ_{em} = 800 \sim 830 nm and high quantum efficiencies (QEs) of 30% \sim 40%, leading to an NIR light power $\sim\!\!3\times$ superior to prevailing NIR emitters. The ultralong λ_{em} and high QE stem from a coordinated energy transfer and an optimized electronic delocalization around Eu(II). This work provides a cost-efficient computational approach for discovering phosphors with desired emissions.

INTRODUCTION

Developing an efficient near-infrared (NIR, 700–1100 nm) phosphor is a long-standing quest for many cutting-edge applications, such as medical diagnostics, food detection, security monitoring, and machine vision. Although Cr(III) activation in many host materials yields NIR emissions, its intrinsic spin-forbidden d-d transition limits the absorption efficiency to well below 30%.^{2,3} Conversely, Eu(II) has widely been used as an efficient luminescent center in lighting, displays, security, and photovoltaics due to its dipole-allowed 5d-to-4f transition.^{4–7} Despite displaying various emission colors, the vast majority of known Eu(II)-activated phosphors exclusively cover the visible spectrum region, and only a handful emit beyond 700 nm (summarized in supplemental information; Table S2). The state-of-the-art Eu(II) NIR phosphor, $K_3LuSi_2O_7$:Eu(II), exhibits an emission peak (λ_{em}) at 740 nm with a quantum efficiency (QE) of 15% when excited at 460 nm. ⁸ The development of Eu(II) NIR phosphors poses a critical challenge due to a trade-off between long λ_{em} and high QE. This trade-off inherently impedes the extension of already well-established Eu(II)-activated phosphors to the remote monitoring/sensing sector. The significant yet required energy gap between excitation and emission sources, namely the Stokes shift, is fundamentally associated with energy losses, which reduce the QE through non-radiative processes. The excitation and emission energies of 5d-to-4f transitions are very host sensitive and hold a multi-dimensional dependency, implying that numerous host matrices remain untested today. Consequently, the sustainable and fast development of Eu(II) phosphor with ultralong λ_{em} and high QE necessitates a practical

Progress and potential

- Traditionally, a combination of phenomenological theories with quantum mechanical calculations has remained computationally costly and incredibly system dependent. This prediction model represents the most remarkable advance over the last 2 decades in predicting Eu(II) luminescence with an error of ca.
 7.0 nm. This unique prediction capability will accelerate the discovery of novel luminescent materials.
- We demonstrate that ultrapseudo Stokes shift via coordinated Eu-Eu energy transfer circumvents energy losses that are intrinsic to large Stokes shifts. This work overcomes the trade-off between ultralong emission and high quantum efficiency. More fundamentally, the low-cost and well-defined nature of the luminescence descriptors developed in this work materialize an in silico propertytargeted design capability for Eu(II)-activated phosphors and introduce significant sustainability for future research and development of energy-saving lighting technologies.





understanding of lanthanide rare earths' optical transitions and, more importantly, an algorithmic evaluation of the 5*d*-to-4*f* optical transition energies.

In essence, the 4f-to-5d transition energy of Eu(II) results from a perturbation of the free Eu ion open-shell states due to the in-crystal bonding. In theory, chemical, electronic, and geometrical factors around Eu(II) dictate the emission wavelength of Eu(II) and are commonly parameterized via the nephelauxetic effect and crystal-field splitting. Hitherto, predicting these energy levels remained unsuccessful due to intricate quantum processes, such as electron correlation interactions and electron delocalization. As a result, the design of NIR Eu(II) phosphors has primarily been led by trial-and-error experimentation, wherein sustainable photoluminescence-guided developments remain impalpable. An accurate prediction of Eu(II) emission wavelength undoubtedly will present an unprecedented design capability to develop practical NIR Eu(II) phosphors and, more generally, 5d-to-4f based phosphors.

In this work, starting from the covalo-electrostatic model, 10 we parameterize well-defined chemical, electronic, and geometrical descriptors into a weighted harmonic covalo-electrostatic parameterization (HCEP) emission prediction model. The model quantifies the relative energy difference between the 4f and 5d levels of Eu(II) using five readily accessible descriptors and predicts the Eu(II) emission energy with a root-mean-square error (RMSE) of only 0.03 eV (7.0 nm). Using the HCEP model, a sustainable photoluminescence-guided screening of 223 nitride materials in the Inorganic Crystal Structure Database (ICSD) 11 identifies five potential NIR Eu(II) phosphors. Merging advanced experimental validations with chemical site engineering, we demonstrate the potentiality of the HCEP model to accelerate spectral tuning by designing (Sr1-xBax)3Li4Si2N6:Eu(II) with ultralong emission peaks (800 \sim 830 nm) and high QEs of 30% \sim 40%. This study initiates an *in silico* property-targeted design of Eu(II) emitters, identifies a state-of-the-art ultralong Eu(II) phosphor at 830 nm (Table S3), and materializes a crucial component for remote sensing technologies.

RESULTS AND DISCUSSION

Harmonic covalo-electrostatic parameterization model and prediction of NIR Eu(II) phosphors

The emission energy ($E_{\rm em}$) of the Eu(II) 5d-to-4f transition is approximated by the energy difference between the excited $4f^65d^1$ and the ground $4f^7$ energy levels of the in-crystal Eu(II) activator. However, obtaining accurate solutions to these energy levels ($4f^65d^1$ and $4f^7$) remains challenging for periodic solids. The covaloelectrostatic interaction model correlates the shift of these in-crystal energy levels relative to the free ion (Figure 1A). The central field covalency around the Eu(II) predominantly affects the tail of the expanded and non-shielded 5d wavefunction. Consequently, other than the initial lattice's Madelung potential, only a fraction of the activator-host interactions affects the well-shielded 4f energy levels.

The presence of polarizable ligands around Eu(II) leads to the centroid shift (ϵ_c) of the 5d centroid position (5d_c) from its free ion position. The centroid shift in its low parameter formulation $(\epsilon_c) \sim \frac{CN\alpha_{sp}}{P_{A-N}^c}$ correlates with the average bond length (ℓ_{A-N}) between the activator site (A) and the nitrogen site (N) (for nitride materials), the nearest neighbor (1NN) coordination number (CN) around the activator, and the host's spectroscopic polarizability (α_{sp}). Fundamentally, ϵ_c describes the two-electron correlation between the localized 5d electrons and the delocalized ligands' electrons; and α_{sp} and ℓ_{A-N} account for the strength of the A-N ionic bonding character. The free anion polarizability of nitrogen is substantially larger than other anions

¹Fujian Key Laboratory of Materials Genome and College of Materials, Xiamen University, Xiamen 361005, China

²Department of Nanoengineering, University of California San Diego, San Diego, CA 92093-0448,

³College of Optical and Electronic Technology, China Jiliang University, Hangzhou 310018, China

⁴These authors contributed equally

⁵Lead contact

^{*}Correspondence: z9wang@eng.ucsd.edu (Z.W.), ongsp@eng.ucsd.edu (S.P.O.), rjxie@xmu.edu.cn (R.-J.X.)

https://doi.org/10.1016/j.matt.2022.04.009



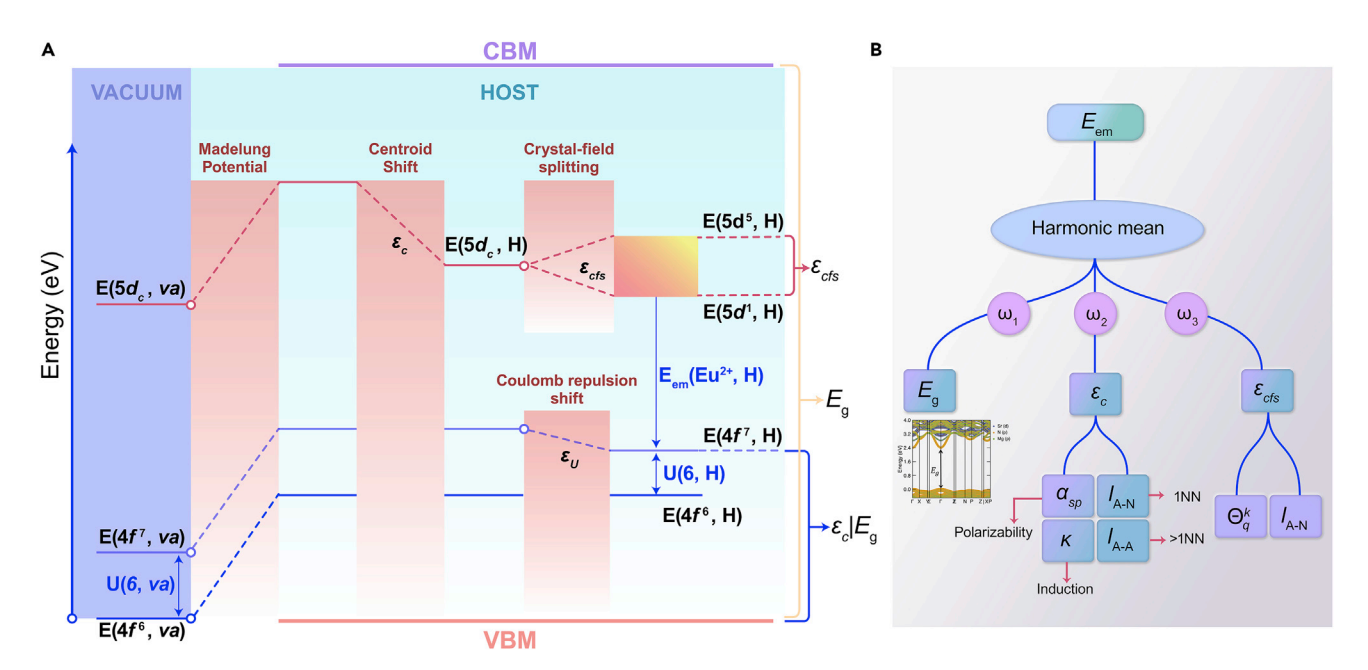


Figure 1. The harmonic covalo-electrostatic parameterization (HCEP) model

(A) The free (va) and in-crystal (H) energy level diagram of Eu. Binding a free Eu impurity into a lattice leads to an upward shift of the 4f and 5d levels due to a positive contribution of the lattice's Madelung potential. The local environment around Eu(II) alters the 5d centroid position ($5d_c$), quantified by the centroid shift (ϵ_c) and induces a geometry-dependent crystal-field splitting (ϵ_{cfs}). The energy level of $E(4f^0$, H) varies with the Coulomb repulsion energy U(6, H) and is relatively quantified by the Coulomb repulsion shift (ϵ_c). The emission energy (E_{em}) is defined as the energy difference between the excited $4f^65d^1$ and the ground $4f^0$ energy levels of the in-crystal Eu(II). VBM is the valence band maximum, and CBM is the conduction band minimum, and their energy difference is the host band gap (E_g). Note, the notation $\epsilon_c|E_g$ means that $E(4f^0$, H) depends on both parameters. (B) A schematic of the developed HCEP model for predicting the emission peak (E_{em}) of Eu(II) phosphors.

 $(\alpha_{\rm sp}({\rm F}^-)=0.557~{\rm Å}^3<\alpha_{\rm sp}({\rm O}^{2-})=0.802~{\rm Å}^3<\alpha_{\rm sp}({\rm N}^3-)=1.100~{\rm Å}^3)$, and it results in two important characteristics: (1) A-N covalent interactions would significantly contribute to ϵ_c while reducing the f-d interactions, 13 and (2) farther species 14 (e.g., A = Ca, Sr, Ba beyond 1NN) around the activator would selectively add a considerable influence on the 5d energy levels while minimally affecting the 4f electrons. 15,16 In this work, we improve the covalo-electrostatic model by incorporating the contributions of farther neighbors to the A-N covalency and extend the 1NN ϵ_c using the host's inter-A sites distances ($I_{\rm A-A}$) and the host's degree of condensation (κ). The former introduces additional covalent terms in ϵ_c beyond 1NN, and the latter regulates the inductive effect of counter-cations (refer to sections S1.4 and S1.5 in the supplemental information). The non-shielded nature of the localized 5d electrons induces strong crystal-field interactions quantified by the crystal-field splitting of the 5d levels, denoted by ϵ_{cfs} (Figure 1A), as conventionally defined under the point charge electrostatic model, $\frac{17}{\epsilon_{cfs}} \propto \frac{\Theta_q^k}{\beta_{n-N}^k}$, where $\frac{1}{\epsilon_n}$ is the angular parameter defined by the point group symmetry of the AN $_x$ (x = CN) polyhedron (section S1.6).

As stated earlier, the absolute location of $4\vec{l}'$ ($E(4\vec{l}', H)$) is less sensitive to its surrounding environment than the 5d levels. Previous reports have noted that the host band gap (E_g) has a partial contribution to $E(4\vec{l}', H)$ of the in-crystal Eu(II). For example, preceding measurements show that the Eu 4f binding energies (U(6, H) in Figure 1A) of structurally similar materials are governed by their respective lattice polarizability, which in return is governed by the host band gap (E_g). On the other hand, the binding energies of chemically diverse hosts are correlated to the experimentally measured 5d centroid shift. The U(6, H) is therefore





conditionally dominated by the antagonist competitiveness between primary effect (ϵ_c) and secondary effects (E_g) (refer to section S1.7). To average the contributions of all three parameters dictating $E_{\rm em}$, the weighted harmonic mean of E_g , ϵ_c , and ϵ_{cfs} is utilized (Figure 1B). The emission energy is then expressed as follows:

$$E_{em} \propto \left(\frac{w_1 E_g^{-1} + w_2 \epsilon_c^{-1} + w_3 \epsilon_{cfs}^{-1}}{w_1 + w_2 + w_3}\right)^{-1},$$

where w_1 , w_2 , and w_3 are fitted weights. All predicted emission energies will be reported as their respective emission peak wavelengths (λ_{em} , nm), allowing a convenient comparison between experimental and computational results.

To parameterize the HCEP model, we develop a dataset of 40 experimentally measured Eu(II) emission peaks ($\lambda_{\rm em}^{\rm exp}$) of diverse chemistries (Table S4). The principal component analysis shows that the dataset exhibits a broad descriptor ($E_{\rm g}$, $\alpha_{\rm sp}$, $I_{\rm A-N}$, $I_{\rm A-A}$, κ) distribution (Figure S8). Figure 2A plots the predicted emission wavelength ($\lambda_{\rm em}^{\rm pred}$) with respect to the experimental values ($\lambda_{\rm em}^{\rm exp}$) for the 40 emission peaks of Eu(II). The achieved RMSE is only 7.0 nm (0.03 eV). The leave-one-out cross-validated RMSE in the predicted emission wavelength ($\lambda_{\rm em}^{\rm pred}$) is 10 nm (0.04 eV) (Figure S9). We proceed to identify NIR Eu(II) phosphors by selecting relevant nitride materials from the ICSD in terms of their elemental compositions. This yields 223 candidates, which were then structurally optimized using density functional theory (DFT) calculations (see experimental procedures). Utilizing the HCEP model, five candidates (Sr₃Al₂N₄, Sr₃Li₄Ge₂N₆, Ca₄LiB₃N₆, Ca₃Li₄Si₂N₆, and Sr₃Li₄Si₂N₆) were directly predicted to yield NIR Eu(II) emission ($\lambda_{\rm em}$ > 700 nm) (Figures 2B and 2C and Table S5).

Experimental validation and photoluminescence properties

To validate the HCEP model, we synthesized the five Eu(II)-activated candidates and characterized their optical properties. The phase purity of these five compounds was confirmed by X-ray diffraction (XRD) Rietveld refinements (Figure S10 and Table S6). Ca₄LiB₃N₆ has a single Ca site of 8c Wyckoff position, and Sr₃Al₂N₄ has two nonequivalent Sr sites (8e/4c). Sr₃Li₄Si₂N₆, Ca₃Li₄Si₂N₆, and Sr₃Li₄Ge₂N₆ are isostructural monoclinic phases with two nonequivalent Sr/Ca sites, namely, 4h and 2b/2a.²¹ Eu(II)-doping content was fixed at dilute 0.1% to avoid reabsorption and concentration quenching (Figure S11). The emission spectra of these five compounds were measured under 450 nm excitation, and the excitation spectra were monitored at their respective emission peaks (λ_{em}), shown in Figures 3A, 3B, and S12. Ca₄LiB₃N₆:Eu_{8c}(II), having a unique Ca site, yields a single emission peak at 714 nm. The other four compounds' emission spectra with two Eu(II) nonequivalent sites were Gaussian-deconvoluted into two sub-bands, i.e., $Sr_3Al_2N_4$:Eu(II) ($\lambda_{em}^{exp}/\lambda_{em}^{pred} = 636/647$ and 701/706 nm), $Sr_3Li_4Si_2N_6$:Eu(II) ($\lambda_{em}^{exp}/\lambda_{em}^{pred} = 670/675$ and 800/799 nm), $Ca_3Li_4Si_2N_6$:Eu(II) ($\lambda_{em}^{exp}/\lambda_{em}^{pred}$ $\lambda_{\rm em}^{\rm pred} = 700/690$ and 782/765 nm), and $Sr_3Li_4Ge_2N_6$:Eu(II) ($\lambda_{\rm em}^{\rm exp}/\lambda_{\rm em}^{\rm pred} = 668/669$ and 795/801 nm) (Figure S13 and Table S5). These measured emission peaks agree well with the HCEP model's predictions.

In particular, $A_3 \text{Li}_4 C_2 \text{N}_6$:Eu(II) (A = Ca, Sr; C = Si, Ge) exhibits the longest emissions ($\lambda_{\text{em}} > 780$ nm). The photoluminescence (PL) spectra at room temperature show a substantial overlap between the short ($\lambda_{\text{em}}^{\text{S}}$) and long ($\lambda_{\text{em}}^{\text{I}}$) emission sub-bands, and the PL spectra at low-temperature (10 K) confirm the dual-emission character of $A_3 \text{Li}_4 C_2 \text{N}_6$:Eu(II) (Figures 3C and S14). The HCEP model predicts that $\lambda_{\text{em}}^{\text{I}}$ and $\lambda_{\text{em}}^{\text{S}}$ originate from Eu(II) located at 4h (Eu_{4h}) and 2b/2a (Eu_{2b/2a}), respectively, where $I_{\text{A-A}}$ and $I_{\text{A-N}}$ are shorter for Eu_{4h} (Figure 2C and Table S4). More importantly, the



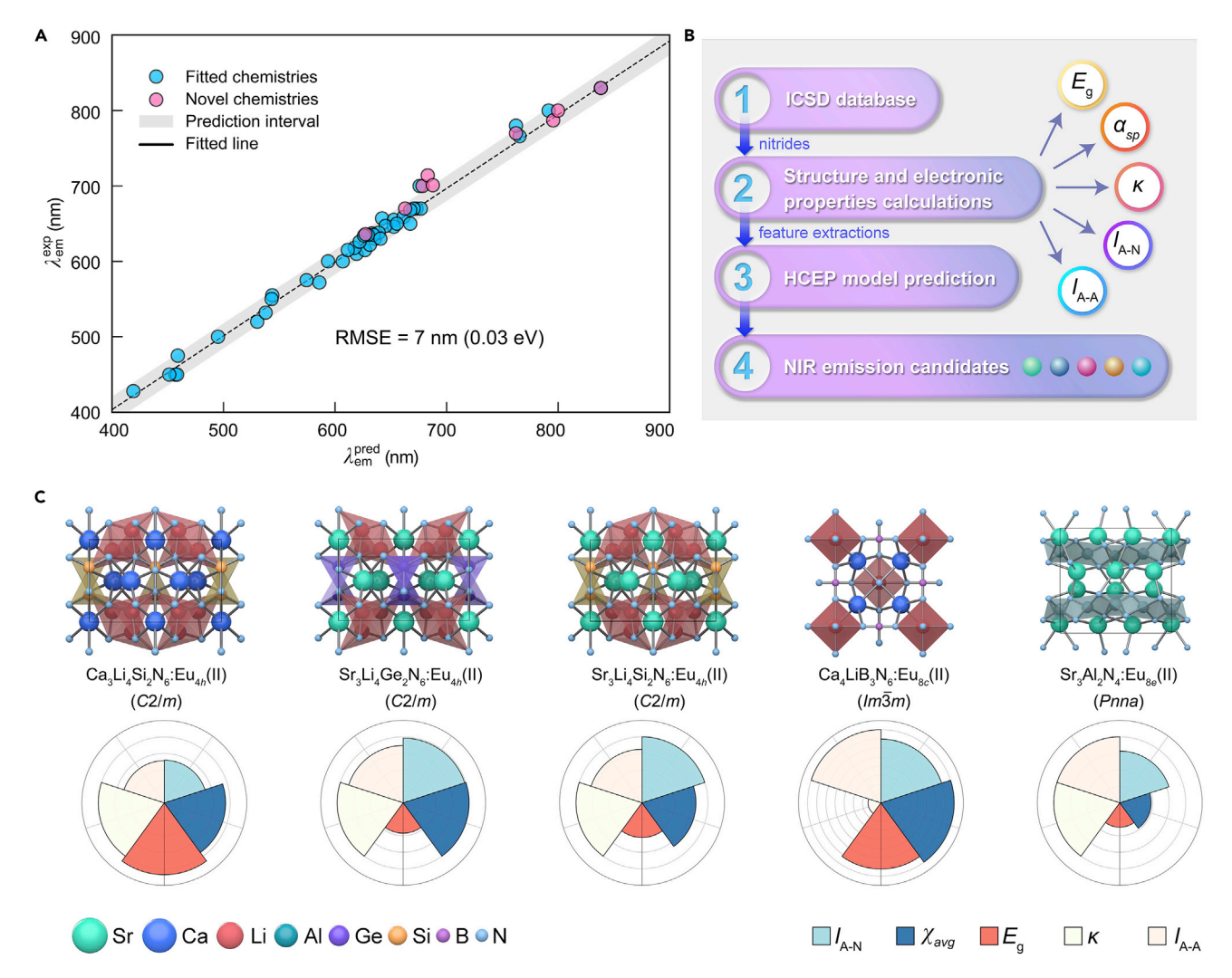


Figure 2. Identification of NIR Eu(II) phosphors

(A) The predicted emission peaks (λ_{em}^{pred}) using the HCEP model as a function of the experimental values (λ_{em}^{exp}). RMSE refers to the square root of the average squared difference between λ_{em}^{pred} and λ_{em}^{exp} .

(B) HCEP model aided high-throughput screening workflow.

(C) Crystal structure and space group of the five NIR Eu(II) phosphor candidates: $Ca_3Li_4Si_2N_6$: $Eu_{4h}(II)$, $Sr_3Li_4Ge_2N_6$

ultralong emission is characterized by a large ϵ_{cfs} and ϵ_c (reduced I_{A-N} and I_{A-A} in Ca₃Li₄Si₂N₆:Eu_{4h}(II)), or by a large ϵ_c and a low E_g in Sr₃Li₄(Si/Ge)₂N₆:Eu_{4h}(II) or by an increased induction (low κ) as observed in Ca₄LiB₃N₆:Eu_{8c}(II) (Figure 2C). The wavelength-dependent excitation and emission spectra of A₃Li₄Si₂N₆:Eu(II) (A = Ca, Sr) show that the absorption of Eu_{4h} overlaps with the emission of Eu_{2a/2b} (Figures S15 and S16). Sr₃Li₄Si₂N₆:Eu(II) possesses the largest absorption(Eu_{4h})-emission(Eu_{2b}) overlap (λ_{ex} = 450 nm), suggesting an efficient Eu_{2b}-Eu_{4h} energy transfer.

The radiative decay curves at 10 K were measured to understand the nature of Eu(II) optical transitions in $A_3Li_4C_2N_6$:Eu(II) (A = Ca, Sr; C = Si, Ge) (Figures 3D, S14C, and S14D). Two distinct radiative lifetime regimes are observed: $Eu_{2b/2a}$ ($\tau < 530$ ns) and Eu_{4h} ($\tau > 2,300$ ns). More importantly, the fast radiative lifetimes ($Eu_{2b/2a}$) are roughly twice as fast as a typical Eu(II) decay lifetime ($\tau \sim 1,000$ ns). The substantially long



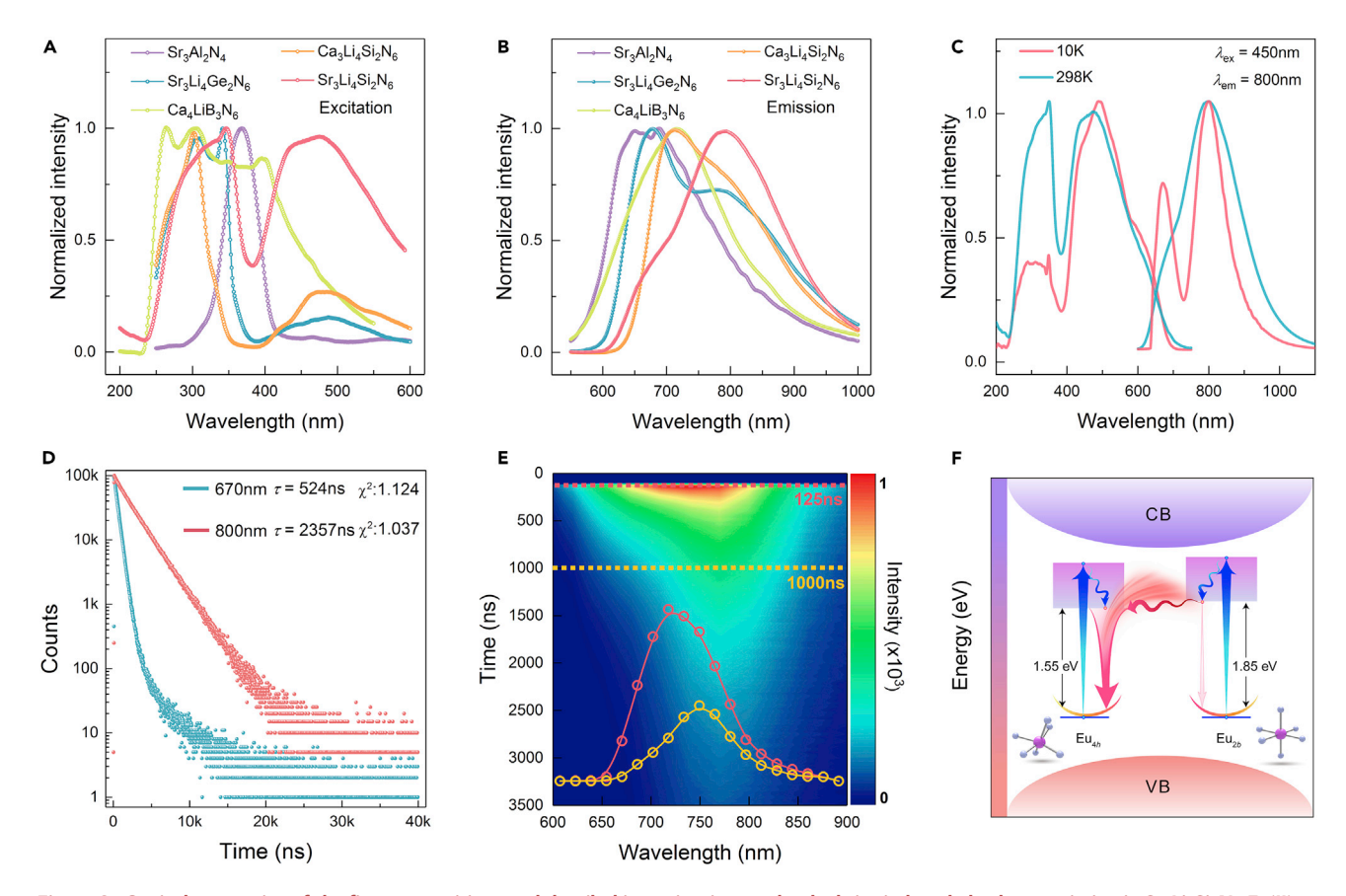


Figure 3. Optical properties of the five compositions and detailed investigation on the dual-site induced ultralong emission in Sr₃Li₄Si₂N₆:Eu(II)

- (A) Normalized excitation spectra monitored at each phosphor's respective longest λ_{em} .
- (B) Normalized emission spectra excited at 450 nm.
- (C) Normalized excitation and emission spectra of Sr₃Li₄Si₂N₆:Eu(II) at 10 and 298 K.
- (D) Emission decay curves monitored at both Sr_{2b} site (670 nm) and Sr_{4h} site (800 nm) in $Sr_3Li_4Si_2N_6$:Eu(II).
- (E) Time-resolved luminescence spectra of $Sr_3Li_4Si_2N_6$: Eu(II) under 450-nm pulse laser excitation. The inset spectra are obtained at a delay time of 125 and 1,000 ns, respectively.
- (F) Illustration of the energy transfer from Eu_{2b} to Eu_{4h} in $Sr_3Li_4Si_2N_6$: Eu(II), and insets show the nearest neighbor local coordination. Note, the locations of Eu(II) $4\vec{f'}$ levels in the illustration are merely qualitative and does not reflect their absolute energy levels.

radiative decay times from Eu_{4h} can be attributed to the additional time required for the energy transfer and the increased delocalization of the 5d electron due to a shorter I_{A-A} distance.²² Time-resolved luminescence spectroscopy (see Figure 3E) measured at 450-nm pulse laser excitation shows an initial short-wavelength emission (recorded at 125 ns), followed by a longer-wavelength emission recorded at 1,000 ns. This significant temporal delay further confirms the existence of an Eu_{2b} - Eu_{4h} energy transfer as schematically depicted in Figure 3F.

The QEs of $Sr_3Li_4Si_2N_6$:Eu(II), $Ca_3Li_4Si_2N_6$:Eu(II), and $Sr_3Li_4Ge_2N_6$:Eu(II) are measured to be 40%, 3%, and 1%, respectively. From Figure 3A, we observe that $Sr_3Li_4Si_2N_6$:Eu(II) has the most efficient excitation at 450 nm, followed by $Ca_3Li_4Si_2N_6$:Eu(II) and $Sr_3Li_4Ge_2N_6$:Eu(II), which partially explains the high QE of $Sr_3Li_4Si_2N_6$:Eu(II). The ratios between the respective integrated areas of $\lambda_{\rm em}^{\rm l}$ and $\lambda_{\rm em}^{\rm s}$ ($R(\lambda_{\rm em}^{\rm l}/\lambda_{\rm em}^{\rm s})$) are 9.16, 2.83, and 1.91 for $Sr_3Li_4Si_2N_6$, $Ca_3Li_4Si_2N_6$, and $Sr_3Li_4Ge_2N_6$, respectively, as shown in Figure S13) suggest that $Sr_3Li_4Si_2N_6$:Eu(II) has a high emission intensity in the long emission region, a crucial requirement for practical applications.



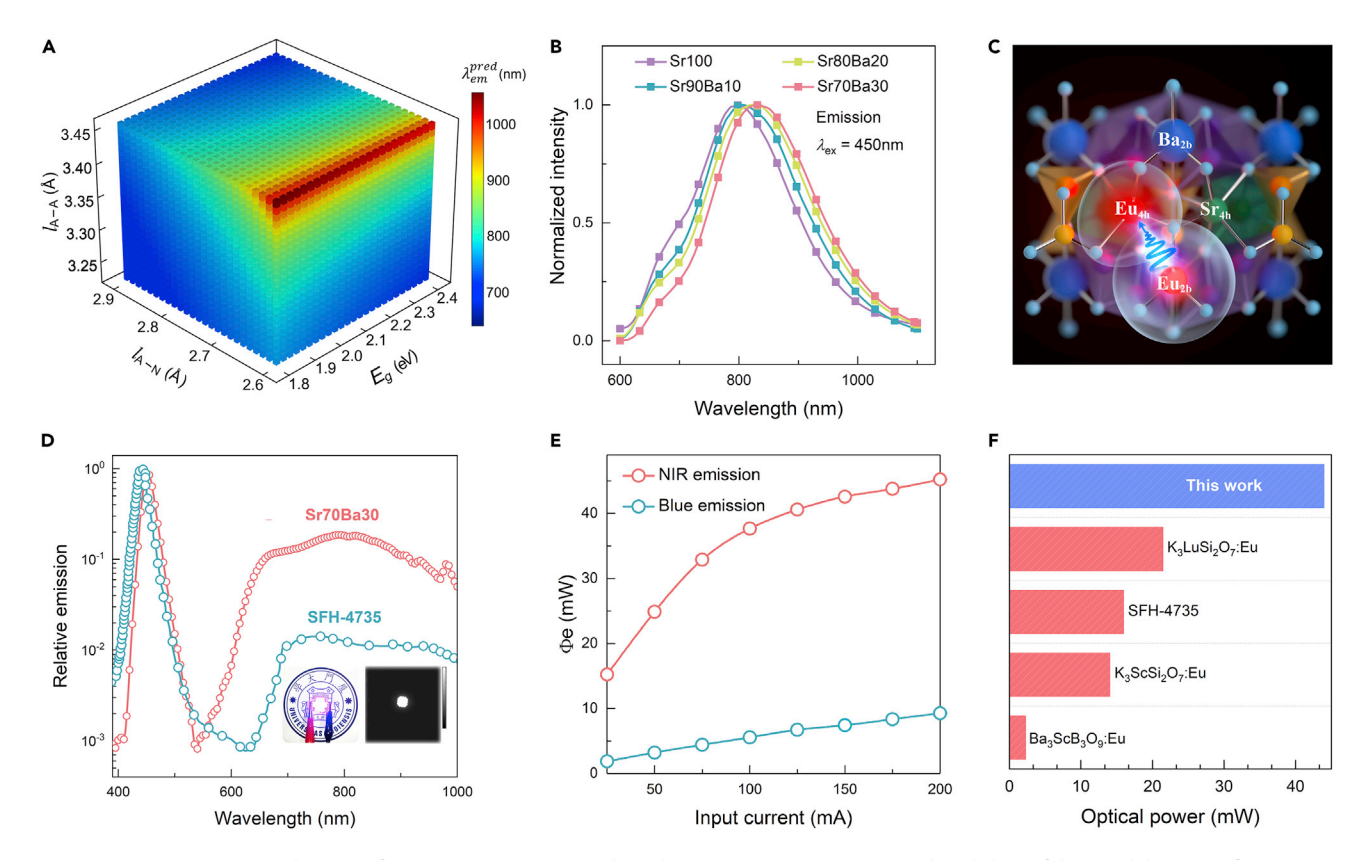


Figure 4. Parametric spectral tuning of Sr₃Li₄Si₂N₆:Eu(II) via an algorithmic site engineering approach and the as-fabricated device performance

- (A) Photoluminescence (PL) design map involving three of the most influential descriptors (E_g , I_{A-N} , I_{A-A}) for $Sr_3Li_4Si_2N_6$: $Eu_{4h}(II)$.
- (B) Emission spectra of $(Sr_{1-x}Ba_x)_3Li_4Si_2N_6$: Eu(II) (x=0,0.1,0.2,0.3) when excited at 450 nm, where x=0 is abbreviated as Sr100, and so forth.
- (C) A schematic diagram of Sr/Ba/Eu sites and the interactions in Sr70Ba30.
- (D) PL spectrum of fabricated NIR light source with Sr70Ba30 at a driven current of 200 mA, compared to the spectrum of SFH-4735 from OSRAM (OSLON Black Flat (IR broad band emitter) 120° Version 1.0). Inset showcases the switch-on device taken by visible and NIR cameras, respectively. (E) Optical power of blue and NIR emission as a function of input current.
- (F) Comparison of optical power between Sr70Ba30 and previously reported Eu(II) NIR phosphors, including the Cr(III)-activated SFH-4735.8,27,28

We conclude that the aforementioned large overlap of Eu_{4h} absorption and Eu_{2b} emission in $Sr_3Li_4Si_2N_6$:Eu(II) (Figure S15) increases the emission efficiency of Eu_{4h} through a coordinated energy transfer. The small difference of the Shannon radii between Sr(II) (1.18 and 1.26 Å for CN = 6 and 8) and Eu(II) (1.17 and 1.25 Å for CN = 6 and 8) and the close proximity of Sr cations around Sr ure usual in a favorable Sr orientation, which reduces the energy of the lowest Sr orbital, Sr while the relatively long radiative lifetime (r = 2,357, 2,617, 2,702 ns for $Sr_3Li_4Si_2N_6$: $Eu_{4h}(II)$, $Eu_{4h}(II)$, $Eu_{4h}(II)$, and $Eu_{4h}(II)$, and $Eu_{4h}(II)$, respectively) suggests a relatively minimized $Eu_{4h}(II)$ and $Eu_{4h}(II)$ in $Eu_{4h}(II)$ (section $Eu_{4h}(II)$) in $Eu_{4h}(II)$ (section $Eu_{4h}(II)$) and $Eu_{4h}(II)$ in $Eu_{4h}(II)$ (section $Eu_{4h}(II)$) as the most promising Eu(II) NIR phosphor to date.

Parametric spectral tuning using the HCEP model

To optimize the photoluminescence of $Sr_3Li_4Si_2N_6$: $Eu_{4h}(II)$, we conducted an algorithmic site engineering as shown by the photoluminescence design map in Figure 4A. Here, we resolved the HCEP model around three critical parameters: E_g , I_{A-N} , and I_{A-A} . The predicted emission peak upon these hypothetical structural variations varies from 600 to 1,000 nm when E_g , I_{A-N} , and I_{A-A} change from 1.8 to 3.0 eV, 2.6 to 2.9 Å, and 3.2 to 3.5 Å, respectively. This photoluminescence (PL) design map





suggests that a simultaneous decrease of $E_{\rm g}$ and increase of $I_{\rm A-A}$ would result in a longer emission peak. The partial substitution of Sr by Ca or Si by Ge is predicted to produce a shorter emission wavelength (Figure S17), which is consistent with our experimental findings (Figure S18). Given that Ba has a larger radius than Sr, the substitution of Sr with Ba would simultaneously increase $I_{\rm A-A}$ (lattice expansion) and decrease $E_{\rm g}$ due to the larger atomic orbitals of Ba and the conduction band minimum character of $A_{\rm 3}Li_{\rm 4}Si_{\rm 2}N_{\rm 6}$ (A d-orbitals) (Figure S19). The synergetic effect of $I_{\rm A-A}$ and $E_{\rm g}$ further delocalizes the 5d electron and therefore results in a longer emission wavelength.

Solid solutions of $(Sr_{1-x}Ba_x)_3Li_4Si_2N_6$: Eu(II) were then synthesized, and the maximum solubility of Ba was found to be 30% (x = 0.3) (Figure S20). At 450-nm excitation, the emission wavelength of these solid solutions (Figure 4B) gradually redshifts from 800 to 830 nm with increasing Ba concentration. The Gaussian-deconvoluted emission spectrum of (Sr_{0.7}Ba_{0.3})₃Li₄Si₂N₆:Eu(II) (abbreviated Sr70Ba30) is composed of two emission peaks (673 and 833 nm in Figure S21). To understand the luminescence behavior of Sr70Ba30, DFT calculations were conducted to determine the site preference of Ba/Eu in Sr₃Li₄Si₂N₆. We find that Ba fully occupies the larger polyhedron at the 2b site ($V_{2b} = 26.80 \text{ Å}^3$; $V_{4h} = 24.68 \text{ Å}^3$), while Sr occupies the remaining 4h sites. Interestingly, we note that the occurrence of the 2b and 4h Wyckoff positions are 1/3 and 2/3, respectively, and it explains the 30% maximum solubility of Ba in $(Sr_{1-x}Ba_x)_3Li_4Si_2N_6$. Beyond a Ba concentration of ~1/3, the 4h positions would have to accommodate for a much larger Ba ion, making the compound thermodynamically unstable. This structural analysis of the phase stability of Ba-doped Sr₃Li₄Si₂N₆ is consistent with our DFT predictions (Table S7). The close Eu dopant formation energies (-0.149 meV/atom at Ba_{2h} and 0.125 meV/atom at Sr_{4h} sites) indicate that Eu(II) simultaneously occupies both 2b and 4h sites, hence preserving the crucial occurrence of the Eu_{2b}-Eu_{4h} energy transfer responsible for the efficient ultralong emission (Figure 4C). The inductive effect created by Ba_{Sr} (due to Ba's lower electronegativity) (1) further increases the AN_x covalency (the sum bond order [SBO] around Sr is 2.0 and 1.87 in Sr70Ba30 and Sr100, respectively), and (2) decreases the host $E_{\rm q}$, so (1) and (2) induce the observed redshift of 30 nm. The QE for Sr70Ba30:Eu(II) is measured to be 30%. The reduction of QE with an increase of Ba can be attributed to two factors: (1) the electron-phonon coupling of the excited states of EuBa and EuSr are different, and that reduces the synchronized resonance of both sites, 23 and (2) the reduction of E_{q} (Table S7) leads to an increased thermal ionization of the shorter emission wavelength site.²⁴

Performance of the NIR device

A prototype NIR light device was demonstrated by integrating Sr70Ba30 with a blue LED chip (maximum current of 200 mA). The inset of Figure 4D showcases the switch-on device taken by visible (left) and NIR (right) cameras, respectively. Under a forward bias current of 200 mA, the recorded photoluminescence (PL) spectrum covers the entire region from 600 to 1,000 nm (Figure 4D), and it matches well with the sensitivity of Si-based camera sensors. Sha seen in Figure 4E, the NIR light power increases with the input current from 25 to 200 mA, and it achieves an optimum of 44 mW at 200 mA. Simultaneously, the blue light also shows a suitable light power for objects detection and spatial localization. In comparison, comparable commercial products yield an optical power on the order of 16 mW, emitting between 600 and about 1,050 nm, when driven at 350 mA (Figure 4D). Consequently, Sr70Ba30 presents a superior emission bandwidth with an optical power roughly x superior to the commercially available device. More importantly, our prototype device outperforms all previously reported Eu(II) NIR phosphors (Figure 4F and



Table S8). 8,27,28 Also, the Sr100-based NIR device exhibits an optical power of 46 mW when driven at 200 mA (Figure S22). Finally, we showcase the integration of the developed NIR device in diverse applications, such as night vision surveillance and oxyhemoglobin saturation detection, which is often regarded as the fifth vital sign (Figure S23). Our NIR devices are also well suitable for applications of iris recognition (810 nm), monitoring (830 nm), and payment systems (830 nm), hence demonstrating the market scalability and societal impact of NIR phosphors and the importance of advancing their fundamental science.

Conclusion

In this work, by mapping experimental emission energies with DFT calculated host's structural, chemical, and electronic properties, we have described the impact of the Eu(II)-host interactions on the 5*d*-to-4*f* energy gap and predicted Eu(II) emission energy via a low-cost HCEP of key descriptors. A HCEP-driven high-throughput screening of 223 chemically targeted nitrides in the ICSD has identified five Eu(II)-activated NIR phosphors. The Sr₃Li₄Si₂N₆:Eu(II) (Sr100) phosphor, a promising prototype benefiting from a coordinated energy transfer and beneficial electronic localization due to a reduced Sr-Sr separation, shows ultralong emission (800 nm) and high QE of 40%. We have implemented the HCEP model as a photoluminescence tuner to design the state-of-the-art Eu(II) NIR phosphor. The simultaneous reduction of band gap and Sr-Sr separation through Ba substitution has led to (Sr_{0.7}Ba_{0.3})₃Li₄Si₂N₆:Eu(II) with an extended emission at 830 nm and NIR light power of 44 mW. We envision that this work will aid the design of Eu(II) phosphors for emerging applications.

EXPERIMENTAL PROCEDURES

Resource availability

Lead contact

The detailed methods including both theoretical calculations and experimental methods can be found in the following parts. It is recommended to contact the lead contact directly for further information and requests for resources and materials: Rong-Jun Xie (rjxie@xmu.edu.cn).

Materials availability

This study did not generate new unique reagents, or there are restrictions to availability.

Data and code availability

All data associated with this study is made publicly available, including the DFT calculation, reformulated centroid shift model, and harmonic covalo-electrostatic parametrization of emission energy.

Density functional theory calculation

All DFT calculations were performed using the Vienna *ab initio* simulation package (VASP) within the projected-augmented wave method. 29,30 The generalized gradient approximation Perdew-Burke-Ernzerhof (PBE) functional revised for solids (PBEsol) 31 was used for structure relaxation of host materials. The plane wave energy cutoff was 520 eV. The electronic energy and structure relaxation were converged to 10^{-5} eV and 0.01 eV/Å, respectively. The Brillouin zone was sampled with a k-point grid density of 1,000 per reciprocal atoms. 32 All crystal structure manipulations and data analysis were carried out using the Python Materials Genomics package. 33 Band gaps of all host materials were calculated using the parameters in line with the Materials Project and previous works, 20,34,35 where the PBE functional 36 was





adopted. The more accurate screened hybrid Heyd-Scuseria-Ernzerhof functional ^{37,38} was used to calculate the host band gap of the most promising candidates. A large supercell with lattice parameters of at least 10 Å in each crystallographic direction was constructed for the Eu(II)-activated hosts, which corresponds to an Eu(II) concentration of less than 5%. PBE calculations with a Hubbard U parameter of 2.5 eV³⁹ for Eu(II) were used for structure relaxation and total energy calculations. The SBO of the chemical bonds was calculated by using the density derived electrostatic and chemical (DDEC6)⁴⁰ method with electron and spin magnetization density distributions calculated with VASP.

Reformulated centroid shift model

In theory, the centroid shift originates from a two-electron crystal-field interaction, whereas physically and mathematically, no radial boundary is defined. Consequently, the two-electron crystal-field interaction can be expanded beyond the first-shell environment to include the A-A interaction. Here, this interaction (denoted by ϵ_c^{A-A}) is proposed to adopt the following form:

$$\epsilon_c^{A-A} = -\alpha_{sp}e^2 \sum_k \frac{1}{I_{A-A}^{2k+4}} [\langle r^k \rangle]^2$$
 (Equation 1)

The A-N interaction accounts for A atoms that are directly bonded to N^{3-} anions with average polarizability α_{sp} . The A-A interaction, however, is prone to the overall lattice electrostatic field. To account for this difference, the lattice's degree of condensation (κ) is treated as a dependent variable of a generalized logistic function modulating the inductive strength of countercations among different hosts:

$$f_{damp}(\kappa) = \frac{1}{1 + e^{-\beta \kappa}}$$
 (Equation 2)

 β is a fitted parameter and defines the spatial-dependency growth rate of the Coulombic screening. Figure S24 depicts the general scheme to formulate the first and second shell centroid shift expression:

$$\epsilon_c^{A-N} = \alpha_{sp} \sum_{i=1}^{2} \omega_i^{A-N} \frac{(i+1)}{l_{A-N}^{2i+4}}$$
 (Equation 3)

$$\epsilon_c^{\text{A-A}} = \alpha_{sp} \sum_{i=1}^{2} f_{damp}^i(\kappa) \omega_i^{\text{A-A}} \frac{(i+1)}{f_{\text{A-A}}^{2i+4}}$$
 (Equation 4)

$$\epsilon_c = \omega^{A-N} \epsilon_c^{A-N} + \omega^{A-A} \epsilon_c^{A-A}$$

where, the dipole-dipole interaction is represented for i=1, and the covalent interaction (second term in Equation SI4) is approximated with a Lennard-Jones type of potential for i=2, and ω_i^{A-N} and ω_i^{A-A} are fitted weights. Finally, the linear relationship of $\alpha_{\rm sp}$ against the inverse square of the average cation electronegativity χ_{avg} requires the fitting of new parameters since the current parameters ($\alpha_{sp}^N=0.87+\frac{18.76}{\chi_{avg}^2}$) were derived while assuming the validity of Equation S5 in the supplemental information (section S1.2).

Harmonic covalo-electrostatic parametrization of emission energy

Given the relatively small dataset used in the development of the harmonic covaloelectrostatic parametrization model, we utilized the leave-one-out cross-validation where the number of folds equals the number of instances in our dataset, i.e., 40. The computed RMSE between the predicted emission wavelengths and the experimentally measured ones is 10 nm, which is small and close to the RMSE (7.0 nm,





RMSE = $\sqrt{\frac{1}{N}}\Sigma_{i=1}^{N}(\lambda_{pred}^{i}-\lambda_{exp}^{i})^{2}$) of the fully trained model and confirms the validity of our model. To further validate the robustness of our prediction model, we computed the predicted wavelength of the five newly discovered host candidates at each k-fold iteration as shown in Figure S18A. Then we averaged the 40 predicted emission wavelengths ($\Sigma^{\frac{\lambda_{pred}^{pred}}{k}}$) and compared it to their measured emission wavelengths (Figure S18). The average predictions are still close to the measured ones, substantiating the accuracy of the HCEP model. More details on the development of the model can be found in the supplemental information.

Experimental methods

The NIR phosphors were synthesized by using binary nitride raw materials of Ca₃N₂ (99%, Cerac), Sr_3N_2 (99.5%, Cerac), Ba_3N_2 (99.7%, Cerac), Li_3N (99.5%, Sigma-Al-2) drich), BN (99.9%, Denka), AlN (F-grade, Tokuyama), Si₃N₄ (SN-E10, UBE), and EuN (99.9%, Materion). The raw materials were mixed according to the appropriate nominal stoichiometric ratio and thoroughly grounded in a silicon nitride mortar in a glove box. Then, the mixtures were transferred into tungsten crucibles and fired in a horizontal tube furnace under a N2-10%H2 atmosphere. Eu(II) doped Sr3Al2N4, $Ca_4LiB_3N_6$, $Sr_3Li_4Si_2N_6$ /(Sr_7Ba) $_3Li_4Si_2N_6$, $Ca_3Li_4Si_2N_6$, and $Sr_3Li_4Ge_2N_6$ were prepared at 1,000°C for 4 h, 1,200°C for 4 h, 900°C for 6 h, 900°C for 4 h, and 900°C for 4 h, respectively. After sintering, the samples were cooled at a rate of 2°C/min to room temperature. Finally, the as-sintered samples were pulverized for performance characterizations. The XRD patterns were collected by a powder X-ray diffractometer (D8 Advance, Bruker, Germany). The photoluminescence (PL) spectra were measured by a fluorescence spectrometer (FLS980, Edinburgh Instruments, UK) at 10 and 298 K. The decay curves were collected using a FLS980 spectrometer with a pulse laser of 450 nm as the excitation source. The timeresolved luminescence spectra were obtained by collecting decay curves monitored from 550 to 1,100 nm with a step wavelength of 25 nm. The QE was measured with an absolute PL quantum yield spectrometer (Quantaurus-QY, Hamamatsu Photonics, Tokyo, Japan). The prototype IR spectrometer was fabricated by coating the mixture of epoxy resin and IR phosphors on a blue LED of 1 W (3030, λ_{em} = 450 nm). The weight ratio of NIR phosphor and epoxy resin was fixed exactly at 1:2. The absolute spectra were recorded using a UV-VIS-NIR spectrophotocolorimeter (HASS-2000, Everfine, Hangzhou, China) under a bias current ranging from 25 to 200 mA. The photographs were taken with a digital camera (EOS 5D Mark II, Canon) or an NIR camera (InGaAs C12471-03).

SUPPLEMENTAL INFORMATION

Supplemental information can be found online at https://doi.org/10.1016/j.matt. 2022.04.009.

ACKNOWLEDGMENTS

This work is supported by the National Natural Science Foundation of China (Nos. 51832005 and U2005213) and the National Science Foundation, Ceramics Program (No. 1911372). The computational resources were provided by the Extreme Science and Engineering Discovering Environment (XSEDE) supported by the National Science Foundation (No. ACI1548562), the Triton Super Computer Center (TSCC) at the University of California, San Diego, and the National Energy Research Scientific Computing Center (NERSC). We show sincere thanks to Yi Zhang from Xi'an Hongyu Opto-Electrical Company, Ltd., for the IR pc-LED device evaluations. S.L. acknowledges Chonggeng Ma's helpful discussions.





AUTHOR CONTRIBUTIONS

S.L. conducted the experiments and measurements, analyzed the characterizations, and prepared the manuscript. M.A. and Z.W. constructed the emission model, performed theoretical calculations, analyzed data, and prepared the manuscript. C.C. gave suggestions to the theoretical calculations. L.W. gave comments on the performance evaluations of NIR emitters. S.P.O. supervised the computational methodology and edited the paper. R.-J.X. held the project and edited the paper. All the authors discussed the results and contributed to the paper.

DECLARATION OF INTERESTS

The authors declare no competing interests.

Received: December 7, 2021 Revised: February 7, 2022 Accepted: April 6, 2022 Published: May 4, 2022

REFERENCES

- 1. Xiang, H., Cheng, J., Ma, X., Zhou, X., and Chruma, J.J. (2013). Near-infrared phosphorescence: materials and applications. Chem. Soc. Rev. 42, 6128-6185.
- 2. Huang, W.-T., Cheng, C.-L., Bao, Z., Yang, C.-W., Lu, K.-M., Kang, C.-Y., Lin, C.-M., and Liu, R.-S. (2019). Broadband Cr³⁺, Sn⁴⁺-doped oxide nanophosphors for infrared mini lightemitting diodes. Angew. Chem. Int. Ed. 58, 2069-2072.
- 3. Jia, Z., Yuan, C., Liu, Y., Wang, X.-J., Sun, P., Wang, L., Jiang, H., and Jiang, J. (2020). Strategies to approach high performance in Cr³⁺-doped phosphors for high-power NIR-LED light sources. Light: Sci. Appl. 9, 86.
- 4. Wang, L., Xie, R.-J., Suehiro, T., Takeda, T., and Hirosaki, N. (2018). Down-conversion nitride materials for solid state lighting: recent advances and perspectives. Chem. Rev. 118, 1951-2009.
- 5. Li, J., Wang, L., Zhao, Z., Sun, B., Zhan, G., Liu, H., Bian, Z., and Liu, Z. (2020). Highly efficient and air-stable Eu(II)-containing azacryptates ready for organic light-emitting diodes. Nat. Commun. 11, 5218.
- 6. Pust, P., Weiler, V., Hecht, C., Tücks, A., Wochnik, A.S., Henß, A.-K., Wiechert, D. Scheu, C., Schmidt, P.J., and Schnick, W. (2014). Narrow-band red-emitting Sr [LiAl₃N₄]:Eu²⁺ as a next-generation LED-phosphor material. Nat. Mater. 13, 891–896.
- 7. Wang, L., Zhou, H., Hu, J., Huang, B., Sun, M., Dong, B., Zheng, G., Huang, Y., Chen, Y., Li, L., et al. (2019). A Eu³⁺-Eu²⁺ ion redox shuttle imparts operational durability to Pb-I perovskite solar cells. Science 363, 265–270.
- 8. Qiao, J., Zhou, G., Zhou, Y., Zhang, Q., and Xia, Z. (2019). Divalent europium-doped nearinfrared-emitting phosphor for light-emitting diodes. Nat. Commun. 10, 5267
- 9. Dorenbos, P. (2003). Energy of the first $4\vec{l} \rightarrow$ 4f⁶5d transition of Eu²⁺ in inorganic compounds. J. Lumin. 104, 239-260.

- 10. Aull, B.F., and Jenssen, H.P. (1986). Impact of ion-host interactions on the 5d-to-4f spectra of lanthanide rare-earth-metal ions, I. A phenomenological crystal-field model. Phys. Rev. B 34, 6640-6646.
- 11. Bergerhoff, G., Hundt, R., Sievers, R., and Brown, I.D. (1983). The inorganic crystal structure data base. J. Chem. Inf. Model. 23,
- 12. Dorenbos, P. (2000). 5d-level energies of Ce³⁺ and the crystalline environment. II. Chloride, bromide, and iodide compounds. Phys. Rev. B 62, 15650-15659.
- 13. Van Pieterson, L., Reid, M.F., Burdick, G.W., and Meijerink, A. (2002). $4f^n \rightarrow 4n^{n-1}5d$ transitions of the heavy lanthanides: experiment and theory. Phys. Rev. B - Condens. Matter Mater. Phys. 65, 1–13.
- 14. Faucher, M., Garcia, D., and Moune, O.K. (1992). Crystal field effects in rare earth compounds. Influence of second nearest neighbours. J. Lumin. 51, 341-350.
- 15. Onuma, H., Yamashita, I., Serizawa, K., Tanno, H., Suzuki, A., Tsuboi, H., Hatakeyama, N., Endou, A., Takaba, H., Kubo, M., et al. (2010). Quantum chemistry and QSPR study on relationship between crystal structure and emission wavelength of Eu²⁺-doped phosphors. J. Soc. Inf. Disp. 18, 301-309
- 16. Etourneau, J., Portier, J., and Ménil, F. (1992). The role of the inductive effect in solid state chemistry: how the chemist can use it to modify both the structural and the physical properties of the materials. J. Alloys Compd. 188, 1–7.
- 17. Görller-Walrand, C., and Binnemans, K. (1996). Handbook on the Physics and Chemistry of Rare Earths, 23 (Elsevier), Chap. 155.
- 18. Thiel, C.W. (2015). Energies of rare-earth ion states relative to host bands in optical materials from electron photoemission spectroscopy. Odonatologica 44, 447-678.
- 19. Dorenbos, P. (2013). Lanthanide 4f-electron binding energies and the nephelauxetic effect

- in wide band gap compounds, J. Lumin, 136, 122-129
- 20. Wang, Z., Ha, J., Kim, Y.H., Im, W.B., McKittrick, J., and Ong, S.P. (2018). Mining unexplored chemistries for phosphors for high-colorquality white-light-emitting diodes. Joule 2, 914-926
- 21. Pagano, S., Lupart, S., Schmiechen, S., and Schnick, W. (2010). Li₄Ca₃Si₂N₆ and Li₄Sr₃Si₂N₆ – quaternary lithium nitridosilicates with isolated $\left[\text{Si}_2\text{N}_6\right]^{10}$ ions. Z. Anorg. Allg. Chem. 636, 1907-1909
- 22. Poort, S.H.M., Meyerink, A., and Blasse, G. (1997). Lifetime measurements in Eu²⁺-doped host lattices. J. Phys. Chem. Sol. 58, 1451-1456.
- 23. Dexter, D.L. (1953). A theory of sensitized luminescence in solids. J. Chem. Phys. 21, 836-850.
- 24. Amachraa, M., Wang, Z., Chen, C., Hariyani, S., Tang, H., Brgoch, J., and Ong, S.P. (2020). Predicting thermal quenching in inorganic phosphors. Chem. Mater. 32, 6256-6265.
- 25. Zhang, M., Wang, L., Meng, L., Wu, X.-G., Tan, Q., Chen, Y., Liang, W., Jiang, F., Cai, Y., and Zhong, H. (2018). Perovskite quantum dots embedded composite films enhancing UV response of silicon photodetectors for broadband and solar-blind light detection. Adv. Opt. Mater. 6, 1800077.
- 26. Reichl, M. (2016). Osram presents the world's first broadband infrared LED.
- 27. Zhang, Q., Wang, X., Tang, Z., and Wang, Y. (2020). A K₃ScSi₂O₇:Eu²⁺ based phosphor with broad-band NIR emission and robust thermal stability for NIR pc-LEDs. Chem. Commun. 56, 4644-4647.
- 28. Tang, Z., Zhang, Q., Cao, Y., Li, Y., and Wang, Y. (2020). Eu²⁺-doped ultra-broadband VIS-NIR emitting phosphor. Chem. Eng. J. 388, 124231.
- 29. Kresse, G., and Furthmuller, J. (1996). Effective iterative schemes for ab initio total-energy



- calculations using a plane-wave basis set. Phys. Rev. B *54*, 11169–11186.
- **30.** Blochl, P.E. (1994). Projector augmented-wave method. Phys. Rev. B *50*, 17953–17979.
- Perdew, J.P., Ruzsinszky, A., Csonka, G.I., Vydrov, O.A., Scuseria, G.E., Constantin, L.A., Zhou, X., and Burke, K. (2008). Restoring the density-gradient expansion for exchange in solids and surfaces. Phys. Rev. Lett. 100, 136406–136414.
- Jain, A., Ong, S.P., Hautier, G., Chen, W., Richards, W.D., Dacek, S., Cholia, S., Gunter, D., Skinner, D., Ceder, G., and Persson, K.A. (2013). Commentary: the Materials Project: a materials genome approach to accelerating materials innovation. APL Mater. 1, 011002– 011011.
- Ong, S.P., Richards, W.D., Jain, A., Hautier, G., Kocher, M., Cholia, S., Gunter, D., Chevrier, V.L., Persson, K.A., and Ceder, G. (2013). Python materials genomics (pymatgen): a robust, open-source python library for materials analysis. Comput. Mater. Sci. 68, 314–319.
- Wang, Z., Chu, I.-H., Zhou, F., and Ong, S.P. (2016). Electronic structure descriptor for the discovery of narrow-band red-emitting phosphors. Chem. Mater. 28, 4024–4031.
- 35. Li, S., Xia, Y.H., Amachraa, M., Hung, N.T., Wang, Z., Ong, S.P., and Xie, R.-J. (2019). Datadriven discovery of full-visible-spectrum phosphor. Chem. Mater. 31, 6286–6294.
- Perdew, J.P., Burke, K., and Ernzerhof, M. (1996). Generalized gradient approximation made simple. Phys. Rev. Lett. 77, 3865–3868.

- Heyd, J., Scuseria, G.E., and Ernzerhof, M. (2003). Hybrid functions based on a screened Coulomb potential. J. Chem. Phys. 118, 8207– 8215.
- 38. Heyd, J., Scuseria, G.E., and Ernzerhof, M. (2006). Erratum: "Hybrid func-tions based on a screened Coulomb potential". J. Chem. Phys. 118, 219906–219911.
- Chaudhry, A., Boutchko, R., Chourou, S., Zhang, G., Gronbech-Jensen, N., and Canning, A. (2014). First-principles study of luminescence in Eu²⁺-doped inorganic scintillators. Phys. Rev. B 89, 155105.
- Manz, T.A. (2017). Introducing DDEC6 atomic population analysis: part 3. Comprehensive method to compute bond orders. RSC Adv. 7, 45552.